Simulation of space-charge effects using a quantum Schrödinger approach

Ji Qiang[*]

Lawrence Berkeley National Laboratory, Berkeley, California 94720, USA

Space-charge effects play an important role in high intensity and high brightness particle accelerators. These effects were generally studied self-consistently by solving the Vlasov-Poisson equations using a particle-in-cell method in the accelerator community. In this paper, we propose an alternative method to simulate the space-charge effects in the accelerator. Instead of solving the Vlasov-Poisson equations, the proposed approach solves the Schrödinger-Poisson equations to study the space-charge effects in accelerators. Using a quantum Schrödinger approach reduces the original problem from six- or four-dimensional phase space down to three or two spatial dimensions. It also provides a possibility to simulate accelerator beam physics on quantum computers by evolving the wave function through quantum gates. Benchmarks of a coasting proton beam through a focusing drift defocusing drift lattice show excellent agreement between the quantum Schrödinger method and the particle-in-cell method.

I. INTRODUCTION

The nonlinear space-charge effects from the Coulomb interactions inside a charged particle beam can degrade beam quality, drive instabilities, generate halo particles and beam losses in high intensity and high brightness accelerators. These effects were generally studied self-consistently by solving the Vlasov-Poisson equations using a particle-in-cell (PIC) method in the accelerator community [1–11]. In the PIC method, a number of macroparticles in six-dimensional or four-dimensional phase space are used to represent the distribution function. These macroparticles are advanced through the accelerator subject to both the external accelerating/focusing fields and the space-charge fields in phase space. The space-charge fields are obtained by solving the Poisson equation on a computational grid. Deposition and interpolation are employed to generate charge density distribution on the grid (from macroparticles) and to obtain the space-charge fields on individual macroparticles from the fields on the grid at each time step. The computational cost is linearly proportional to the number of macroparticles, which makes the simulation effective for many applications.

The PIC method solves the Vlasov-Poisson equations by advancing macroparticles through accelerators in phase space. In this paper, we propose an alternative method to solve the Vlasov-Poisson equations for the study of the space-charge effects in accelerators by using a quantum Schrödinger approach. This approach solves the Schrödinger-Poisson equations in a complex spatial domain and reduces the original problem from six or four dimensions to three or two dimensions. The Schrödinger approach has been used to study plasma physics and cold dark matter in cosmology [12–19]. To the best of our knowledge, this method has not been used in the accelerator beam physics to study the space-charge effects in high energy accelerators, where the relativistic effects are important. In this paper, we adopt this approach to simulating the space-charge effects in the high intensity and high brightness accelerators. Using the quantum Schrödinger method also provides a possibility to simulate classical beam dynamics on quantum computers.

The organization of this paper is as follows: after the Introduction, we present the quantum Schrödinger space-charge model in Sec. II; carry out benchmark between the quantum Schrödinger method and the symplectic PIC method using a coasting proton beam transporting through a focusing drift defocusing drift (FODO) lattice in Sec. III; and draw conclusions in Sec. IV.

II. QUANTUM SCHRÖDINGER SPACE-CHARGE MODEL

The accelerator beam dynamics including space-charge effects is governed by the collisionless Vlasov-Poisson equations:

$$\frac{\partial f}{\partial t} + [f, H] = 0, \tag{1}$$

where $[,]$ is the Poisson bracket, $f(\mathbf{r}, \mathbf{p}, t)$ is the distribution function in four- or six-dimensional phase space, and H is

[*]jqiang@lbl.gov

the Hamiltonian that includes contributions from both external focusing/accelerating potentials and the space-charge Coulomb potential ϕ that can be obtained from the solution of the Poisson equation:

$$\nabla^2 \phi = -\frac{\rho}{\epsilon_0}, \tag{2}$$

where ϵ_0 is the permittivity of vacuum and $\rho = \int d^3 p \times f$ is the charge density distribution.

The above Vlasov-Poisson equation can be approximated using the Husimi representation of the phase space distribution $\mathcal{F}(\mathbf{r}, \mathbf{p}, t) = |\Psi(\mathbf{r}, \mathbf{p}, t)|^2$ [20], where

$$\Psi(\mathbf{r}, \mathbf{p}, t) = \left(\frac{1}{2\pi\hbar}\right)^{3/2} \left(\frac{1}{2\pi\sigma^2}\right)^{3/4} \int d^3 x$$

$$\times \psi(\mathbf{x}, t) \exp\left(-\frac{|\mathbf{r} - \mathbf{x}|^2}{4\sigma^2} - i\frac{\mathbf{p} \cdot \mathbf{x}}{\hbar}\right) \tag{3}$$

and the wave function ψ follows the solution of the Schrödinger equation:

$$i\hbar \frac{\partial \psi}{\partial t} = -\frac{\hbar^2}{2m} \nabla^2 \psi + V(x, y, z)\psi, \tag{4}$$

where the potential V includes both the external potential and the space-charge potential and σ denotes a smoothing parameter. Given the evolution of the wave function, the evolution of phase space distribution $\mathcal{F}$ through the Husimi representation can be approximated as [21]

$$\frac{\partial \mathcal{F}}{\partial t} + [\mathcal{F}, H] = O(\hbar) + O(\hbar^2) + \cdots. \tag{5}$$

The above equation approaches the Vlasov Eq. (1) as $\hbar$ goes to 0. This suggests that by choosing a small $\hbar$ value, the wave function solution of the Schrödinger equation could be used to construct a phase space distribution that approximates the original phase distribution in the Vlasov equation.

Now we consider an accelerator system that consists of a coasting beam and an external quadrupole focusing lattice. The Hamiltonian of the beam using z as an independent variable can be written as [22]

$$\bar{H}(z) = \frac{1}{2}(\bar{p}_x^2 + \bar{p}_y^2) + V(x, y, z), \tag{6}$$

where $\bar{p}_{x,y} = p_{x,y}/p_0$ is normalized momentum, $p_0 = m\gamma_0 v_0$ the reference particle momentum, v_0 the speed of the reference particle, γ_0 the relativistic factor of the reference particle, and V the potential given as

$$V = \frac{1}{2}k(z)(x^2 - y^2) + \frac{1}{2}K\phi, \tag{7}$$

where $k(z) = qg(z)/p_0$ is the effective external quadrupole focusing strength, $g(z)$ is the quadrupole gradient, $K = qI/(2\pi\epsilon_0 p_0 v_0^2 \gamma_0^2)$ is the generalized perveance, and I is the beam current. In this Hamiltonian, the effects of the direct Coulomb electric potential and the longitudinal vector potential are combined together to account for the space-charge effects.

From the above equations, the corresponding Hamiltonian using time t as the independent variable can be obtained as

$$H(t) = \frac{1}{2m\gamma_0}(p_x^2 + p_y^2) + p_0 v_0 V(x, y, z). \tag{8}$$

The Schrödinger equation for the above Hamiltonian can be written as

$$i\hbar \frac{\partial \psi}{\partial t} = -\frac{\hbar^2}{2m\gamma_0} \nabla^2 \psi + p_0 v_0 V(x, y, z)\psi. \tag{9}$$

Here, the relativistic effects on the beam are included in the above equation. This equation can be rewritten using z as the independent variable as

$$i\hbar \frac{\partial \psi}{\partial z} = -\frac{\hbar^2}{2p_0} \nabla^2 \psi + p_0 V(x, y, z)\psi \tag{10}$$

or

$$\frac{\partial \psi}{\partial z} = \frac{i\hbar}{2p_0} \nabla^2 \psi - i\frac{p_0}{\hbar} V(x, y, z)\psi. \tag{11}$$

The above Schrödinger equation can be solved numerically using a Lie-Trotter splitting-operator method [23]. A second-order approximation for one step advance of the wave function can be written as

$$\psi(z + \tau) = e^{\frac{i\hbar\tau}{4p_0}\nabla^2} e^{-i\frac{p_0}{\hbar}V\tau} e^{\frac{i\hbar\tau}{4p_0}\nabla^2} \psi(z), \tag{12}$$

where τ is the advance step size, and each exponential function denotes an operator acting on the wave function ψ for either half step or one step. In the above approximation, we assumed that the potential is constant during one step, which is valid for a quadrupole focusing lattice. The exponential function $e^{\frac{i\hbar\tau}{4p_0}\nabla^2}$ involves the Laplacian partial differential operator that can be solved using a Galerkin spectral method [24–28]. Assuming that the wave function is confined inside a rectangular pipe subject to the boundary conditions:

$$\psi(x = 0, y) = 0 \tag{13}$$

$$\psi(x = a, y) = 0 \tag{14}$$

$$\psi(x, y = 0) = 0 \tag{15}$$

$$\psi(x, y = b) = 0, \tag{16}$$

where a is the horizontal width of the pipe and b the vertical width of the pipe. The wave function can be approximated as

$$\psi(x, y) = \sum_{l=1}^{N_l} \sum_{m=1}^{N_m} \psi_{lm} \sin(\alpha_l x) \sin(\beta_m y), \tag{17}$$

where

$$\psi_{lm} = \frac{4}{ab} \int_0^a \int_0^b \psi(x, y) \sin(\alpha_l x) \sin(\beta_m y) \, dx dy, \tag{18}$$

where $\alpha_l = l\pi/a$ and $\beta_m = m\pi/b$. Using the above spectral representation, the Laplacian operator in the above exponential operator can be replaced by $-\gamma_{lm}^2 = -(\alpha_l^2 + \beta_m^2)$ and the evolution of the wave function in the frequency domain through the first half step can be written as

$$\psi_{lm}(z + \tau/2) = e^{-\frac{i\hbar\tau}{4p_0}\gamma_{lm}^2} \psi_{lm}(z). \tag{19}$$

Using Eq. (17), the wave function $\psi(z + \tau/2)$ in the spatial domain can be obtained from the $\psi_{lm}(z + \tau/2)$ through the inverse sine function transformation. After the first half step, the wave function can be advanced for one step using the potential V as

$$\tilde{\psi}(z + \tau/2) = e^{-i\frac{p_0}{\hbar}V\tau} \psi(z + \tau/2). \tag{20}$$

After this step, the wave function will be advanced through the second half step following the sine function transform of the wave function $\tilde{\psi}(z + \tau/2)$:

$$\psi_{lm}(z + \tau) = e^{-\frac{i\hbar\tau}{4p_0}\gamma_{lm}^2} \tilde{\psi}_{lm}(z + \tau/2). \tag{21}$$

The wave function after one step $\psi(z + \tau)$ can be obtained from the inverse sine transformation equation (17). This process can be repeated for many steps until the beam transports through the lattice.

In order to advance the wave function through Eq. (20), the space-charge potential ϕ in the Hamiltonian potential term V is needed from the solution of the following Poisson equation:

$$\frac{\partial^2 \phi}{\partial x^2} + \frac{\partial^2 \phi}{\partial y^2} = -4\pi\rho, \tag{22}$$

where ϕ is the electric potential, and ρ is the particle density distribution of the beam that can be obtained from the wave function:

$$\rho(x, y) = \int \int e^{-\frac{(x-x')^2}{2\sigma_x^2}} e^{-\frac{(y-y')^2}{2\sigma_y^2}} \psi(x', y')\psi^*(x', y') dx' dy', \tag{23}$$

where σ_x and σ_y are smooth parameters in the x and y dimension respectively.

The electric potential inside the rectangular perfectly conducting pipe follows the same boundary conditions as the wave function:

$$\phi(x = 0, y) = 0 \tag{24}$$

$$\phi(x = a, y) = 0 \tag{25}$$

$$\phi(x, y = 0) = 0 \tag{26}$$

$$\phi(x, y = b) = 0. \tag{27}$$

Given the boundary conditions in Eqs. (24)–(27), the electric potential ϕ and the source term ρ can be approximated using two sine functions following the numerical spectral method:

$$\rho(x, y) = \sum_{l=1}^{N_l} \sum_{m=1}^{N_m} \rho_{lm} \sin(\alpha_l x) \sin(\beta_m y) \tag{28}$$

$$\phi(x, y) = \sum_{l=1}^{N_l} \sum_{m=1}^{N_m} \phi_{lm} \sin(\alpha_l x) \sin(\beta_m y), \tag{29}$$

where

$$\rho_{lm} = \frac{4}{ab} \int_0^a \int_0^b \rho(x, y) \sin(\alpha_l x) \sin(\beta_m y) \, dx dy \tag{30}$$

$$\phi_{lm} = \frac{4}{ab} \int_0^a \int_0^b \phi(x, y) \sin(\alpha_l x) \sin(\beta_m y) \, dx dy, \tag{31}$$

where $\alpha_l = l\pi/a$ and $\beta_m = m\pi/b$. For a smooth function, this spectral approximation has an accuracy whose numerical error scales as $O[\exp(-cN)]$ with $c > 0$, where N is the number of the basis function (i.e., mode number in each dimension) used in the approximation. By substituting the above expansions into the Poisson equation (22) and making use of the orthonormal condition of the sine functions, we obtain

$$\phi_{lm} = \frac{4\pi\rho_{lm}}{\gamma_{lm}^2}, \tag{32}$$

where $\gamma_{lm}^2 = \alpha_l^2 + \beta_m^2$.

In order to solve the Schrödinger equation, one needs to know the initial condition of the wave function. Given the initial phase space distribution $f(\mathbf{r}, \mathbf{p}, 0)$ of the beam, the initial wave function can be constructed from [14]

$$\psi(\mathbf{r}, 0) \propto \sum_{\mathbf{p}} \sqrt{f(\mathbf{r}, \mathbf{p}, 0)} \, e^{i\mathbf{p}\cdot\mathbf{r}/\hbar + 2\pi\phi_{\mathrm{rand},\mathbf{p}}}, \tag{33}$$

where $\phi_{\mathrm{rand},\mathbf{p}}$ is a uniformly distributed random number between zero and one at a given momentum. The inclusion

of the random phase is to avoid the coherence summation of different momentum plane waves.

From the wave function of the Schrödinger equation, one can obtain the second-order moments of the beam in the $x - p_x$ plane as [15]

$$\langle x^2 \rangle = \int \int x'^2 \psi \psi^* dx' dy' \tag{34}$$

$$\langle p_x^2 \rangle = \hbar^2 \int \int \frac{\partial \psi}{\partial x'} \frac{\partial \psi^*}{\partial x'} dx' dy' \tag{35}$$

$$\langle x p_x \rangle = \hbar \, \mathrm{Im} \left(\int \int x' \frac{\partial \psi}{\partial x'} \psi^* dx' dy' \right), \tag{36}$$

where Im denotes the imaginary part of the integral. The second-order moments in the $y - p_y$ plane can be attained by replacing x with y. The emittance of the beam can be calculated using these moments as

$$\epsilon_x = \sqrt{\langle x^2 \rangle \langle (p_x/p_0)^2 \rangle - \langle x(p_x/p_0) \rangle^2} \tag{37}$$

$$\epsilon_y = \sqrt{\langle y^2 \rangle \langle (p_y/p_0)^2 \rangle - \langle y(p_y/p_0) \rangle^2}. \tag{38}$$

III. BENCHMARK EXAMPLES

In this section, we tested the above quantum Schrödinger approach with three examples and compared the simulation results with those from a symplectic particle-in-cell (PIC) solver [29]. In these examples, we simulated a 1 GeV coasting proton beam transporting through a linear periodic quadrupole focusing and defocusing (FODO) channel inside a rectangular perfectly conducting pipe. A schematic plot of the lattice is shown in Fig. 1. It consists of a 0.1 m focusing quadrupole magnet and a 0.1 m defocusing quadrupole magnet within a single period. The total length of the period is one meter. The zero current phase advance through one lattice period is 85.0 degrees. The initial transverse normalized emittance of the proton beam is 1 mm mrad with a 4D Gaussian distribution.

In the first example, we used the above Schrödinger method to simulate the proton beam transporting through five FODO periods without including the space-charge effects. Figure 2 shows the horizontal and vertical root mean square (rms) size, rms momentum, and beam Twiss alpha (e.g., $alpha_x = -\langle x p_x \rangle / \epsilon_x$) evolutions through the lattice from the solutions of the above Schrödinger equation and from the PIC solver. Here, the potential term includes only the external focusing potential. The space-charge Coulomb interactions were not included in both

FIG. 1. Schematic plot of the FODO lattice used in the benchmark examples.

simulations. The aperture size of the rectangular pipe is 12 by 12 mm. The number of grid points are 5120 by 5120 with $\sigma_x/hx = \sigma_y/hy = 30$ and $\hbar/p_0 = 3.0 \times 10^{-8}$. In the quantum representation, momentum is proportional to $\hbar$ and wave number. The maximum momentum that can be attained is set by the $\hbar$ and the largest wave number that can be represented on the computational grid. On one hand, the $\hbar$ should be chosen as small as possible in order to attain good phase space resolution and approximation to the Vlasov equation. This suggests the numerical de Broglie wavelength $2\pi\hbar/p_0$ should be much less than the system physical scale length. On the other hand, the smaller $\hbar$ reduces the attainable momentum for a fixed wave number. The largest wave number in the x or the y direction is given by $\pi N_x/a$ or $\pi N_y/b$. Here, N_x and N_y are the number of grid cells in the x and y dimension respectively. The choice of the $\hbar$ results from a balance of the requirements of accuracy and computational efficiency in the space-charge simulation.

There are four curves in each plot of the above figure. Only two are visible due to the overlap between the quantum solutions and the PIC solutions. The quantum Schrödinger approach agrees with the PIC method very well in this example. Figure 3 shows the scaled rms horizontal and vertical emittance evolutions $[\epsilon(z)/\epsilon(0)]$ through this lattice from both the Schrödinger solver and the PIC solver. Without the nonlinear space-charge forces, the proton beam emittance through a linear focusing lattice should stay constant. Both methods show the constant emittance evolution through the lattice. There are four curves in this figure, two from the quantum Schrödinger solution, two from the PIC simulation. They all overlap with each other in this example.

In the second example, the space-charge effects were turned on for a 100 A proton beam. The depressed phase advance per period is 72.0 degrees for this case. The initial distribution is a rms matched four-dimensional Gaussian distribution including the space-charge effects. Figure 4 shows the horizontal and vertical rms size, rms momentum, and beam Twiss alpha parameter evolutions through the FODO lattice from the solutions of the above Schrödinger-Poisson equations and from the PIC solver. Here, the potential term includes both the external focusing potential and the space-charge potential. The matched rms beam sizes show regular oscillation through the lattice. The rms beam divergence oscillates inside the drifts and decreases inside the quadrupoles. The Twiss parameter alpha oscillates between the horizontal (x) and the vertical (y) dimension through the lattice. There are four curves in each plot of the above figure, two from the quantum Schrödinger solver, two from the PIC solver. The results from the two solvers agree with each other very well and overlap on the top of each other. Figure 5 shows the scaled emittance evolutions through the lattice from the Schrödinger solver and from the PIC solver. Due to the
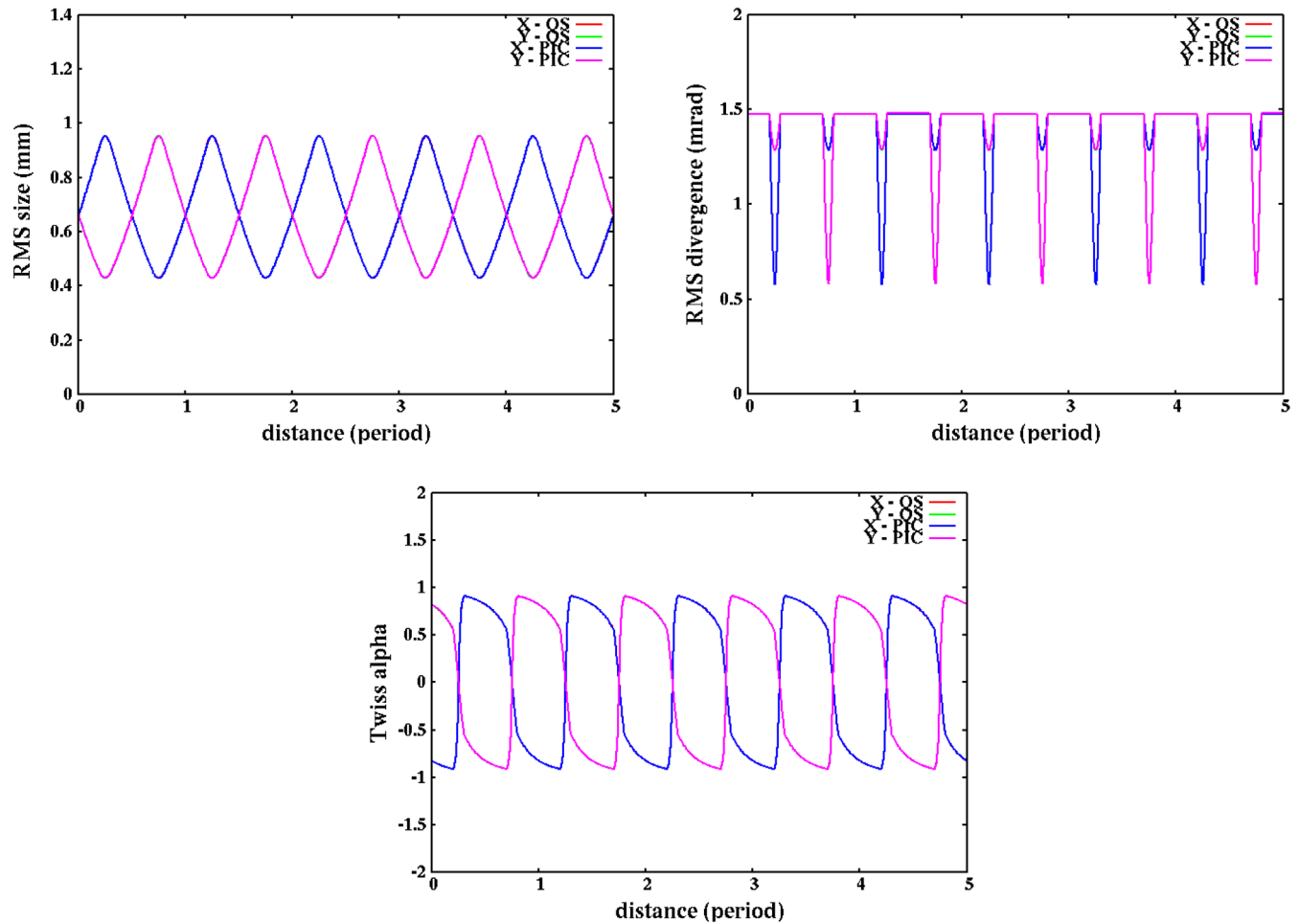
FIG. 2.   Horizontal (x) and vertical (y) rms size (top left), rms momentum (top right), and beam Twiss alpha parameter (bottom) evolution through a five period FODO lattice from the quantum Schrödinger method (red and green) and from the PIC method (blue and magenta) without including the space-charge effects.
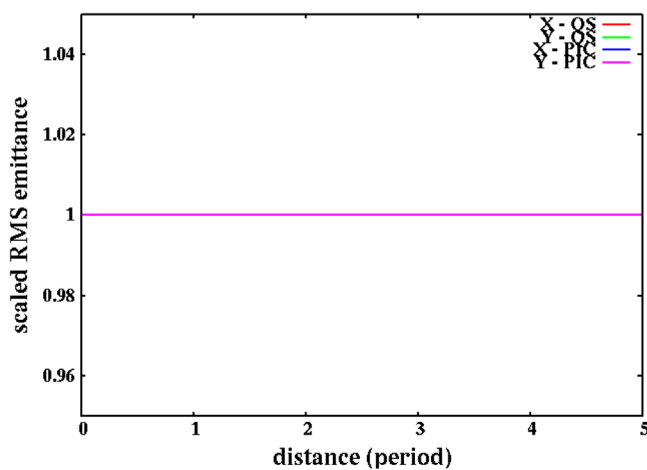

FIG. 3.   Horizontal (x) and vertical (y) rms emittance evolution through a five period FODO lattice from the quantum Schrödinger method (red and green) and from the PIC method (blue and magenta) without including the space-charge effects.

presence of the space-charge effects, the emittances of the proton beam no longer stay constant even with an initial matched distribution. The nonlinear space-charge effects cause small emittance growth in this matched case through the lattice. This slight emittance growth is observed from both the quantum simulation and from the PIC simulation. The relative discrepancy between these two simulations is less than 1%.

In the third example, we introduced a mismatch to the proton beam initial distribution. Here both initial matched horizontal and vertical sigmas were increased by 20% while the divergence sigmas were decreased by about 20%. Figure 6 shows the horizontal and vertical rms size, rms momentum, and beam Twiss alpha parameter evolutions through the lattice from the solutions of the above Schrödinger-Poisson equations and from the solutions of the PIC solver. Here, the potential term in the Hamiltonian includes both the external focusing potential and the space-charge potential from the 100 A beam current. The aperture size of the conducting pipe was increased to 16 by 16 mm
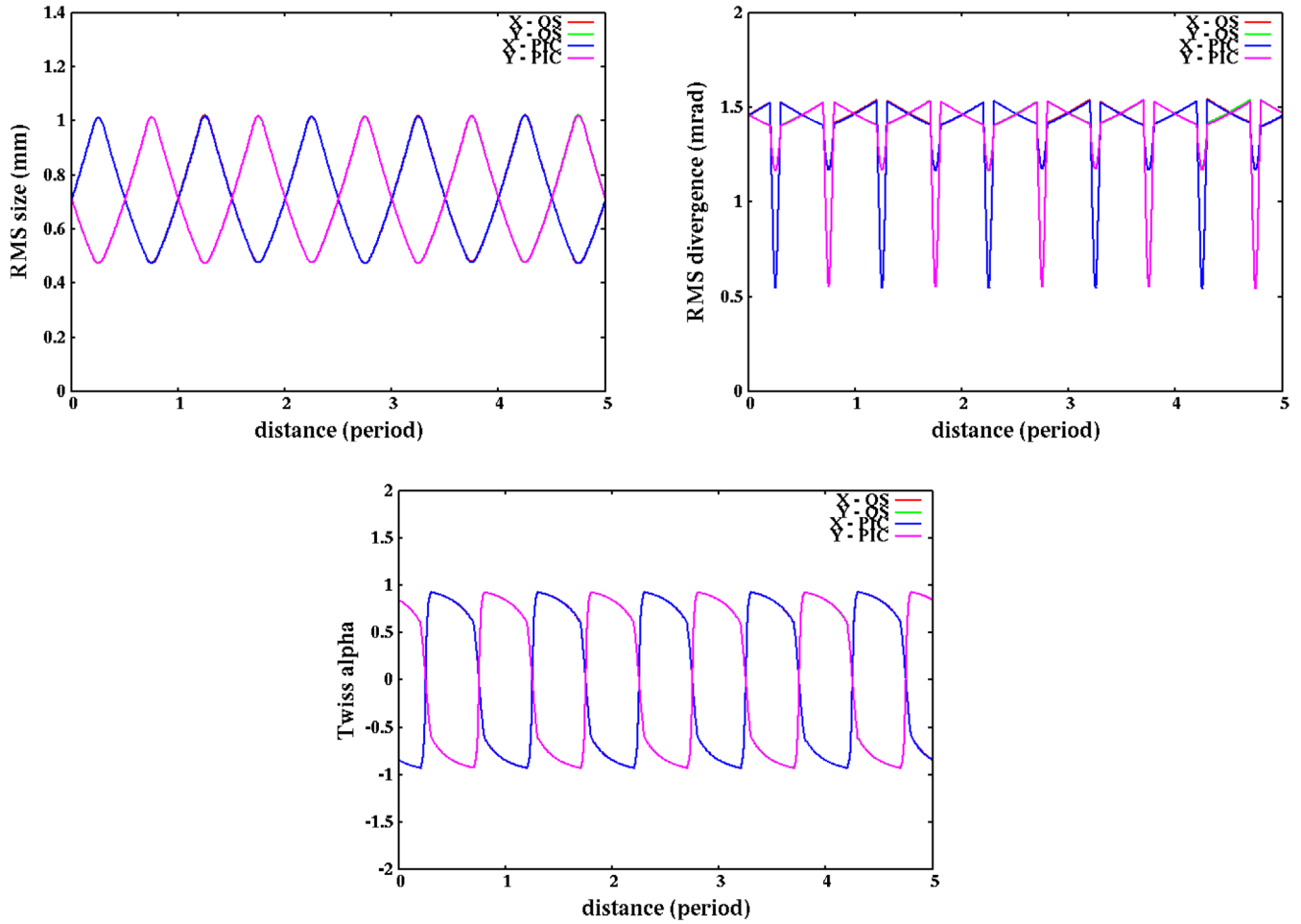
FIG. 4. Horizontal (x) and vertical (y) rms size (top left), rms momentum (top right), and beam Twiss alpha parameter (bottom) evolution through a five period FODO lattice from the quantum Schrödinger method (red and green) and from the PIC method (blue and magenta) with the space-charge effects.
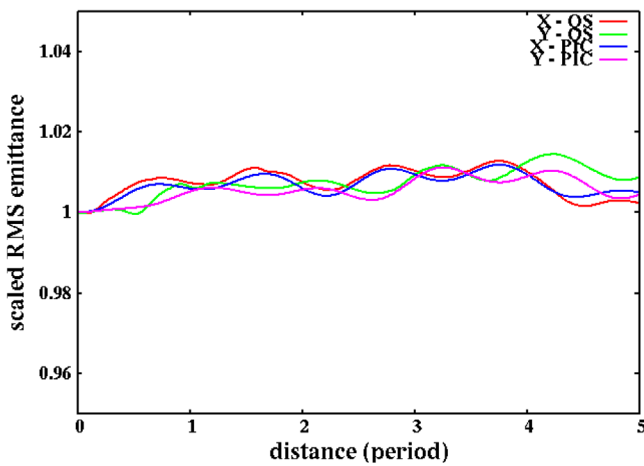

FIG. 5. Four-dimensional normalized rms emittance evolution through a five period FODO lattice from the quantum Schrödinger method (red and green) and from the PIC method (blue and magenta) with the space-charge effects.

to avoid particle losses. The initial mismatched distribution causes proton rms size and divergence growth within the first 50 periods and attains a quasisteady state after 60 periods. The Twiss parameter alpha was not significantly affected by the initial mismatch. There are four curves in each plot of the above figure. Two curves corresponding to the horizontal and vertical dimensions are from the quantum simulation results and two from the PIC simulation results. The quantum simulation results agree with the PIC simulation results very well and the two curves from the quantum simulation overlap the two curves from the PIC simulation. Figure 7 shows the scaled horizontal and the vertical rms emittance evolutions through the lattice from the solutions of the quantum Schrödinger method and from the PIC method. The initial mismatch causes nearly 50% horizontal emittance growth and 30% vertical emittance growth before saturation after 150 lattice periods. Such growth is captured in both the quantum simulation and the PIC simulation. The quantum simulation results agree with those from the PIC simulation very well.
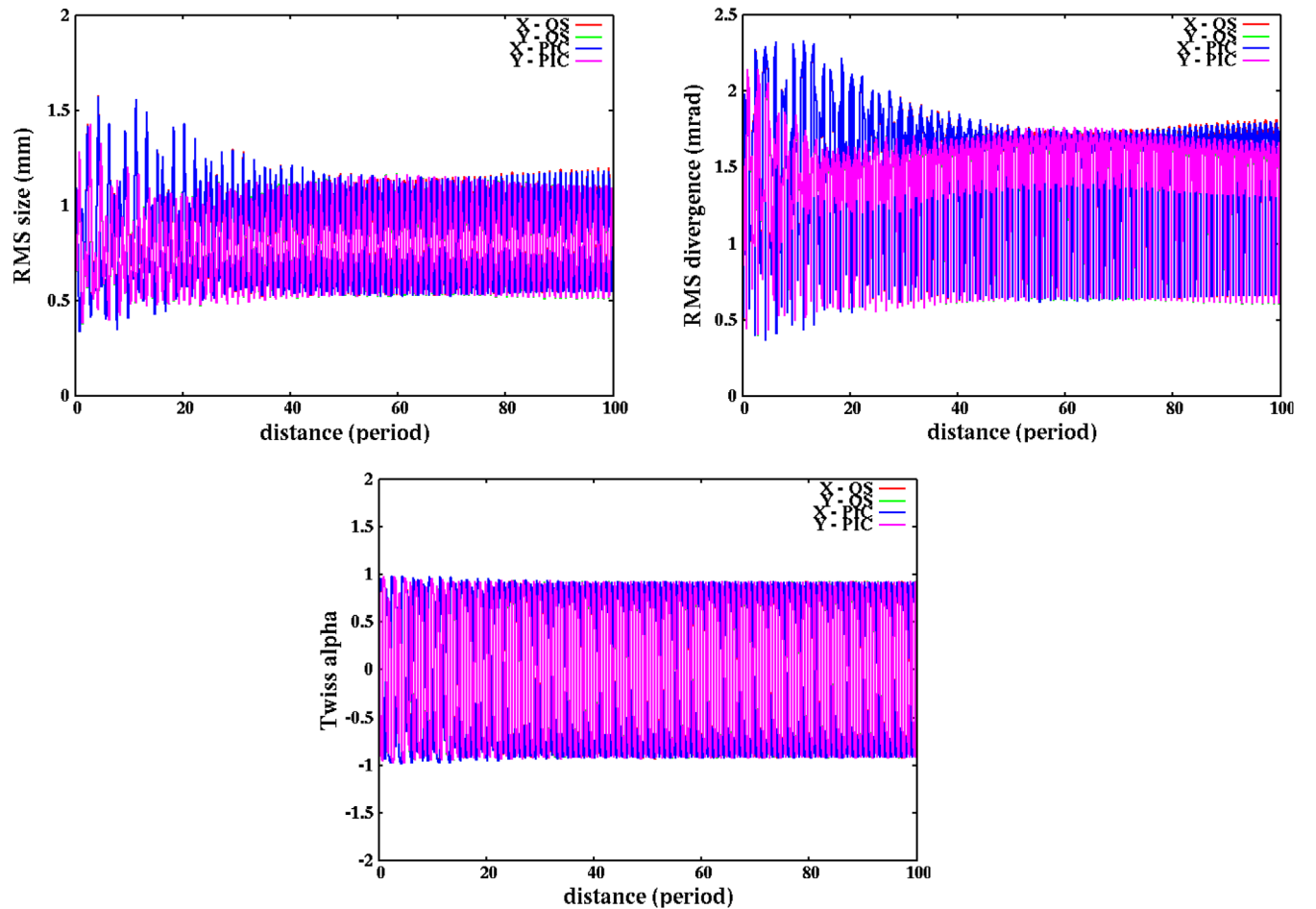
FIG. 6.   Horizontal (x) and vertical (y) rms size (top left), rms momentum (top right), and beam Twiss alpha parameter (bottom) evolution through a five period FODO lattice from the quantum Schrödinger method (red and green) and from the PIC method (blue and magenta) with the mismatched space-charge effects.
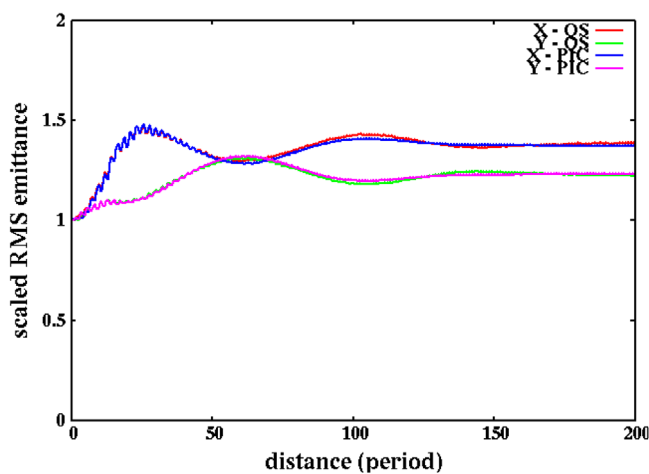

FIG. 7.   Horizontal (x) and vertical (y) rms emittance evolution through a five period FODO lattice from the quantum Schrödinger method (red and green) and from the PIC method (blue and magenta) with the mismatched space-charge effects.

IV. DISCUSSION AND CONCLUSIONS

In this paper, we proposed a quantum Schrödinger approach to simulate space-charge effects in high intensity and high brightness beams of the particle accelerator. The computational cost of this approach scales as $O[N \log(N)]$, where N is the number of grid points. The computational cost of the PIC method scales as $O(N_p)$, where N_p is the number of macroparticles. If the total number of grid points in two or three dimensions is less than the total number of macroparticles in four or six dimensions, the quantum Schrödinger method can be more effective. Meanwhile, using a quantum wave function not only reduces the dimensionality of the problem by half but also provides a possibility to do accelerator beam dynamics simulation on quantum computers. A quantum algorithm has been proposed to solve the Schrödinger equation on quantum computers [30]. That algorithm used the Lie-Trotter splitting method to advance the wave function through multiple quantum gates. It made use of the quantum fast Fourier transform that scales as the $O\{[\log(N)]^2\}$ for the advance

of the kinetic operator. For a quadratic external potential, the total computational cost can scale as $O\{[\log(N)]^2\}$. This method might be extended to include the space-charge effects and will be explored in our future study.

In this paper, we used a high intensity coasting proton beam transporting through a periodic FODO lattice to benchmark the proposed quantum Schrödinger method with a symplectic particle-in-cell solver. Using an example without the space-charge effects, an example with the matched space-charge effects, and an example with the mismatched space-charge effects, we showed that the quantum Schrödinger simulation results agree with the particle-in-cell simulation results very well. This suggests that the quantum Schrödinger method could be used as an alternative approach to study the space-charge effects in high intensity and high brightness beams.

ACKNOWLEDGMENTS

[1] A. Friedman, D. P. Grote, and I. Haber, Phys. Fluids B **4,** 2203 (1992).

[2] H. Takeda and J. H. Billen, Recent developments of the accelerator design code PARMILA, in *Proceedings of the 19th International Linear Accelerators Conference, Chicago, IL, 1998* (NTIS, Springfield, VA, 1998), p. 156.

[3] S. Machida and M. Ikegami, AIP Conf. Proc.**448,** 73 (1998).

[4] F. W. Jones and H. O. Schoenauer, in *Proceedings of the 18th Particle Accelerator Conference, New York, 1999* (IEEE, New York, 1999), p. 2933.

[5] J. Qiang, R. D. Ryne, S. Habib, and V. Decyk, J. Comput. Phys. **163,** 434 (2000).

[6] P. N. Ostroumov and K. W. Shepard, Phys. Rev. ST Accel. Beams **3,** 030101 (2000).

[7] J. D. Galambos, S. Danilov, D. Jeon, J. A. Holmes, D. K. Olsen, F. Neri, and M. Plum, Phys. Rev. ST Accel. Beams **3,** 034201 (2000).

[8] G. Franchetti, I. Hofmann, M. Giovannozzi, M. Martini, and E. Metral, Phys. Rev. ST Accel. Beams **6,** 124201 (2003).

[9] J. Qiang, S. Lidia, R. D. Ryne, and C. Limborg-Deprey, Phys. Rev. ST Accel. Beams **9,** 044204 (2006).

[10] J. Amundson, P. Spentzouris, J. Qiang, and R. Ryne, J. Comput. Phys. **211,** 229 (2006).

[11] http://amas.web.psi.ch/docs/opal/opal_user_guide-2.0.0 .pdf.

[12] P. Bertrand, N. van Tuan, M. Gros, B. Izrar, M. Feix, and J. Gutierrez, J. Plasma Phys. **23,** 401 (1980).

[13] N.-D. Suh, M. R. Feix, and P. Bertrand, J. Comput. Phys. **94,** 403 (1991).

[14] L. M. Widrow and N. Kaiser, Astrophys. J. **416,** L71 (1993).

[15] G. Davies and L. M. Widrow, Astrophys. J. **485,** 484 (1997).

[16] C. Uhlemann, M. Kopp, and T. Haugg, Phys. Rev. D **90,** 023517 (2014).

[17] M. Kopp, K. Vattis, and C. Skordis, Phys. Rev. D **96,** 123532 (2017).

[18] P. Mocz, L. Lancaster, A. Fialkov, F. Becerra, and P.-H. Chavanis, Phys. Rev. D **97,** 083519 (2018).

[19] M. Mina, D. F. Mota, and H. A. Winther, Astron. Astrophys. **641,** A107 (2020).

[20] K. Husimi, Proc. Phys. Math. Soc. Jpn. **22,** 264 (1940).

[21] R. T. Skodje, H. W. Rohrs, and J. Van Buskirk, Phys. Rev. A **40,** 2894 (1989).

[22] R. D. Ryne, Computational methods in accelerator physics, U.S. particle accelerator class note, 2012.

[23] H. F. Trotter, Proc. Am. Math. Soc. **10,** 545 (1959).

[24] D. Gottlieb and S. A. Orszag, *Numerical Analysis of Spectral Methods: Theory and Applications* (Society for Industrial and Applied Mathematics, Philadelphia, PA, 1977).

[25] B. Fornberg, *A Practical Guide to Pseudospectral Methods* (Cambridge University Press, Cambridge, England, 1998).

[26] J. Boyd, *Chebyshev and Fourier Spectral Methods* (Dover Publications, Inc., New York, 2000).

[27] J. Qiang and R. D. Ryne, Comput. Phys. Commun. **138,** 18 (2001).

[28] J. Qiang, Comput. Phys. Commun. **203,** 122 (2016).

[29] J. Qiang, Phys. Rev. Accel. Beams **21,** 054201 (2018).

[30] G. Benenti and G. Strini, Am. J. Phys. **76,** 657 (2008).